RESEARCH ARTICLE

Sodium-Ion Batteries

Energy & Environmental Materials WILEY

Three-Layer Structured SnO_2@C@TiO_2 Hollow Spheres for High-Performance Sodium Storage

Yu Tian, Ping Hu, Ting Zhu, Zhenhui Liu, Guangwu Hu, Congcong Cai, Zelang Jian, Liang Zhou, and Liqiang Mai**

The unsatisfactory conductivity and large volume variation severely handicap the application of SnO_2 in sodium-ion batteries (SIBs). Herein, we design unique three-layer structured SnO_2@C@TiO_2 hollow spheres to tackle the above-mentioned issues. The hollow cavity affords empty space to accommodate the volume variation of SnO_2, while the C and TiO_2 protecting shells strengthen the structural integrity and enhances the electrical conductivity. As a result, the three-layer structured SnO_2@C@TiO_2 hollow spheres demonstrate enhanced Na storage performances. The SnO_2@C@TiO_2 manifests a reversible capacity two times to that of pristine SnO_2 hollow spheres. In addition, *Ex situ* XRD reveals highly reversible alloying and conversion reactions in SnO_2@C@TiO_2 hollow spheres. This study suggests the introduction of a hollow cavity and robust protecting shells is a promising strategy for constructing SIB anode materials.

1. Introduction

Confronted with global energy shortage, the utilization of sustainable energy and development of efficient energy storage devices have become increasingly important. Lithium-ion batteries (LIBs) are essential in portable electronics and electric vehicles. However, extensive application of LIBs is hampered by the limited reserves and rising price of Li.[1-3] Given the moderate cost and plentiful reserves of Na, sodium-ion batteries (SIBs) are expected to complement LIBs in some specific applications in the future.[4-8]

Despite the similar chemical properties of Na and Li, the larger size of Na^+ makes it difficult to apply conventional LIB intercalation anode materials for Na storage.[9,10] Transition metal oxides (TMOs) operated on conversion reaction, such as Fe_2O_3,[11] Co_3O_4,[12] and SnO_2,[13,14] do not confront the above situation and possess high Na storage capacity. Among the TMOs, SnO_2 displays extraordinary high theoretical capacity originated from the intergration of alloying and conversion mechanisms. Especially, the reversible alloying/de-alloying reaction is able to afford a theoretical capacity of 667 mAh g^{-1}. However, the conversion of SnO_2 and generation of solid electrolyte interface (SEI) film cause a large initial capacity loss, leading to low initial Coulombic efficiency (ICE).[15-18] Besides, SnO_2 faces the notorious problem of large volume expansion (400%). Furthermore, as a semiconductor, SnO_2 possesses undesirable low electrical conductivity.[19] Wang *et al.* designed carbon-coated hollow SnO_2/graphene nanocomposites for SIBs, which manifested a capacity of 277 mAh g^{-1} after 100 cycles.[20] Pan *et al.* constructed cactus-like SnO_2/carbon composites, which exhibited enhanced Na storage properties.[21] Yi *et al.* designed a SnO_2@TiO_2 core-shell structure with sufficient free space to buffer the volume fluctuation, showing high capacity and excellent durability.[22] Tian *et al.* prepared TiO_2@SnO_2@C hollow nanobelts for LIBs, which showed high capacity and greatly improved stability.[23] In general, the volume change and conductivity issues of SnO_2 have been well addressed in Li storage, but still exist in Na storage.

To simultaneously overcome the volume change and electrical conductivity issues of SnO_2, three-layer structured SnO_2@C@TiO_2 hollow spheres have been successfully designed herein. The hollow structure could accommodate the volume fluctuation of SnO_2 and shorten the transport paths of Na^+ and electrons.[24] The conductive carbon and mechanically robust TiO_2 shells serve as protecting components to avoid structure collapse and the agglomeration during cycling. The obtained SnO_2@C@TiO_2 hollow spheres demonstrate improved Na storage abilities in terms of capacity, cyclability, and reversibility.

2. Results and Discussion

The synthesis process of three-layer structured SnO_2@C@TiO_2 hollow spheres is briefly presented in **Figure 1**a. First, SnO_2 hollow spheres are produced according to a report by Lou *et al.*[25] The SnO_2 hollow spheres are then wrapped with an ultra-thin polydopamine (PDA) layer to form bilayer SnO_2@PDA hollow spheres.[19] The PDA layer is converted into carbon by annealing in Ar. Then, an amorphous TiO_2 layer is uniformly coated onto SnO_2@C with subsequent annealing, rendering three-layer structured SnO_2@C@TiO_2 hollow spheres.[26]

The crystalline structure of SnO_2@C@TiO_2 and SnO_2 is investigated using X-ray diffraction (XRD). The XRD pattern of SnO_2@C@TiO_2 is

Y. Tian, Dr. P. Hu, Dr. T. Zhu, Dr. Z. Liu, G. Hu, C. Cai, Prof. Z. Jian, Prof. L. Zhou, Prof. L. Mai
State Key Laboratory of Advanced Technology for Materials Synthesis and Processing, Wuhan University of Technology, Wuhan 430070, China
Prof. L. Zhou, Prof. L. Mai
Foshan Xianhu Laboratory of the Advanced Energy Science and Technology Guangdong Laboratory, Xianhu Hydrogen Valley, Foshan 528200, China
E-mail: liangzhou@whut.edu.cn
E-mail: mlq518@whut.edu.cn
The ORCID identification number(s) for the author(s) of this article can be found under https://doi.org/10.1002/eem2.12117.

DOI: 10.1002/eem2.12117

closely similar to that of SnO_2 (Figure 1b) and shows three high-intensity diffraction peaks at 26.4, 33.8, and 51.7°, which can be assigned to the (110), (101), and (211) diffractions of rutile-phase SnO_2 (JCPDS no. 41–1445). Interestingly, the peaks shift to lower angles for both samples (Figure S1), which may be caused by the emerging of oxygen vacancies during annealing.[27] No diffractions from TiO_2 are detected owing to its amorphous feature.

The chemical environments of Sn and Ti are monitored by X-ray photoelectron spectroscopy (XPS). The Sn 3d spectrum of SnO_2 (Figure 1c) presents two notable components at 495.4 (Sn 3d 3/2) and 486.9 eV (Sn 3d 5/2). When compared to pristine SnO_2, the SnO_2@C@TiO_2 shows a ~ 0.2 eV shift toward low binding energy, which may be caused by the generation of oxygen vacancies and increase of electron density on Sn.[28] The Ti 2p XPS spectrum of SnO_2@TiO_2 (Figure S2) displays two obvious peaks at 464.9 and 459.1 eV, corresponding to the 2p 1/2 and 2p 3/2 of Ti(IV). When compared to SnO_2@TiO_2, a red-shift occurs in the SnO_2@C@TiO_2, indicating the generation of oxygen vacancies in the TiO_2 protecting layer of SnO_2@C@TiO_2.[29]

The Raman spectrum of SnO_2@C@TiO_2 (Figure 1d) presents two broad bands at 1351 and 1590 cm^{-1}, which are characteristic for carbon, confirming the existence of carbon in three-layer structured SnO_2@C@TiO_2.[30] The carbon content in SnO_2@C@TiO_2 is calculated using thermogravimetric analysis (TGA). The weight loss below 300 °C is owing to the removal of residue moisture (Figure 1e). The continuously large weight loss at 300 – 500 °C can be ascribed to the combustion of carbon in air. The carbon contents of SnO_2@C@TiO_2 and SnO_2@C are calculated to be 3.89 and 4.06 wt.%, respectively. The weight increase after 550 °C is due to the oxidation of SnO_{2-x} to SnO_2 and TiO_{2-x} to TiO_2. No weight gain is observed in the TGA curve of SnO_2, which further demonstrates the existence of rich oxygen vacancies in SnO_2 and TiO_2 of SnO_2@C@TiO_2 and SnO_2@C.[31] Using inductively coupled plasma (ICP), the Sn/Ti atomic ratio in SnO_2@C@TiO_2 is determined to be 21.8 (Table S1).

The morphology of the products at different synthetic stages is characterized by scanning electron microscopy (SEM) and transmission electron microscopy (TEM). The SnO_2 exhibits a hollow spherical structure with diameters of 250 – 500 nm, and the shell thickness is ~ 50 nm (**Figure 2**a and **2**d). Both the SnO_2@C (Figure 2b and 2e) and SnO_2@C@TiO_2 (Figure 2c and 2f) inherit the original hollow spherical structure of SnO_2. The shell of SnO_2@C is built up with a large number of nanoparticles, and a thin carbon layer with lighter contrast can be clearly discerned on the surface of nanoparticulate shell (Figure 2e). Similarly, a thin coating layer with a thickness of ~ 5 nm can be observed on the surface of SnO_2@C@TiO_2 (Figure 2g). Interlayer spacing of roughly 0.34 nm is discerned in high-resolution TEM (Figure 2g), which is corresponding to the (110) lattice of rutile-phase SnO_2.[32] Selected area electron diffraction (SAED) presents three diffraction rings, in agreement with (110), (101), and (211) planes of SnO_2 in SnO_2@C@TiO_2 (Figure S3). Energy-dispersive X-ray spectroscopy (EDS) mappings confirm the existence of Sn, O, Ti, and C in SnO_2@C@TiO_2 (Figure 2h and 2i). It can be noticed that the Ti and C are uniformly distributed on the SnO_2 hollow sphere, demonstrating the conformal coating.

The N_2 sorption results of SnO_2@C@TiO_2 and SnO_2 are provided in Figure S4. Both samples are highly porous owing to the hollow structure and nanoparticulate shell. Compared to the SnO_2 (57.2 m^2 g^{-1}), the SnO_2@C@TiO_2 possesses a higher surface area (98.8 m^2 g^{-1}). When applied in Na storage, the highly porous SnO_2@C@TiO_2 can provide a large electrode/electrolyte interface, promoting the Na^+ diffusion and facilitating the sodiation/de-sodiation reaction.

The Na storage ability of SnO_2@C@TiO_2 hollow spheres is investigated in half-cells. The cyclic voltammetry (CV) profiles of SnO_2@C@TiO_2 (**Figure 3**a) present a cathodic peak below 0.5 V and a broad anodic peak between 0.5 and 1.5 V. The cathodic peak can be mainly attributed to the conversation of SnO_2 to Sn and subsequent sodiation of Sn to Na_xSn alloy. The intercalation of Na^+ in TiO_2 and carbon may also contribute to the cathodic peak. The anodic peak is associated with the de-alloying of Na_xSn to Sn. The overlapping CV profiles validate the good electrochemical reversibility of SnO_2@C@TiO_2. The CV profiles of SnO_2@C resemble those of SnO_2@C@TiO_2, while the SnO_2 shows a relatively low anodic peak (Figure S5).

Figure 3b presents representative galvanostatic discharge/charge (GCD) profiles of SnO_2@C@TiO_2 at 200 mA g^{-1}. The SnO_2@C@TiO_2 manifests a first discharge capacity of 642 mAh g^{-1} with an ICE of 53.7%. A capacity loss is noticed in the first cycle, which is caused by the generation of SEI film. The control samples, SnO_2@C (38.7%) and SnO_2 hollow spheres (16.4%), present even lower ICE (Figure S6). The SnO_2@C@TiO_2 presents the highest reversible capacity and best cyclic stability among the three samples (Figure 3c). A capacity of 381 mAh g^{-1} is retained for SnO_2@C@TiO_2 after 100 cycles. In contrast, the SnO_2@C and SnO_2 deliver limited capacities of 178 and 165 mAh g^{-1}, respectively. Meanwhile, the Coulombic efficiency of SnO_2@C@TiO_2 rises gradually in the first several cycles and then remains at more than 99.5% throughout the 100 cycles (Figure S6). In addition, the SnO_2@C@TiO_2 also retains a capacity of 190 mAh g^{-1} after 1000 cycles at 1 A g^{-1} (Figure S7) and the long-term cycling does not destroy the hollow spherical structure as demonstrated by the *ex situ* SEM images (Figure S8a-d). The outstanding cycling stability of SnO_2@C@TiO_2 is mainly owing to the robust shell composed of carbon and TiO_2, which can hold the hollow spherical structure and avoid the SnO_2 from aggregation, effectively. However, capacity decay occurs after 30 cycles for the SnO_2@C, because the thin carbon layer is insufficient to protect SnO_2 from structural collapse caused by the volume expansion. As expected, *ex situ* SEM images (Figure S8e and f) show the hollow spherical structure of both SnO_2@C and SnO_2 have been damaged to a certain degree after 50 cycles.

Figure 3d and 3e present the rate performances of the three SnO_2-based samples. The SnO_2@C@TiO_2 demonstrates better rate performance than the other two samples. It delivers capacities of 438.3, 418.4, 396.7, 332.2, and 264.6 mAh g^{-1} at various current densities from 0.05 to 1 A g^{-1}. When the current density turns back to 0.1 A g^{-1}, the capacity recovers to 415.1 mAh g^{-1}. Considering the relatively low weight percentages of TiO_2 and C, the high capacity of SnO_2@C@TiO_2 is mainly contributed from the SnO_2. Although the SnO_2@C delivers a higher capacity of 539.8 mAh g^{-1} at 0.1 A g^{-1}, it drops to 220.7 mAh g^{-1} at 1 A g^{-1}. As for the SnO_2, it displays significantly lower capacities at different current densities. In addition, SnO_2@C@TiO_2 affords much better Coulombic efficiency, especially at the first several cycles. The above electrochemical tests prove that the three-layer hollow structure can significantly improve Na storage performance.

The electrochemical process is further investigated by electrochemical impedance spectroscopy (EIS). All three materials exhibit a quadrant in the high and middle frequencies followed by a line of constant slope in low-frequency range (**Figure 4**a and **4**b), which are related to the

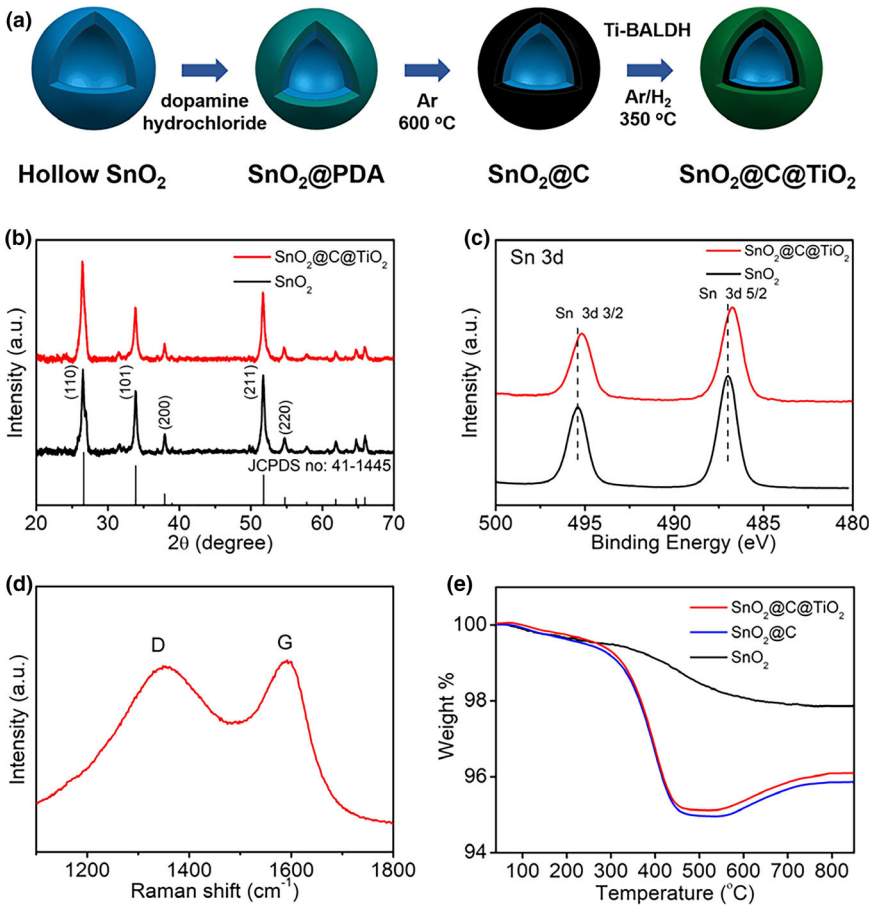

Figure 1. a) Schematic for the construction of three-layer structured SnO_2@C@TiO_2 hollow spheres; b) XRD patterns and c) high-resolution Sn 3d XPS spectra for SnO_2@C@TiO_2 and SnO_2; d) Raman spectrum of SnO_2@C@TiO_2; e) TGA curves of SnO_2@C@TiO_2, SnO_2@C, and SnO_2.

charge transfer resistance and Na^+ diffusivity in the solid phase, respectively. After five discharge/charge cycles, the high-frequency quarter-circles of SnO_2@C@TiO_2 and SnO_2@C become smaller (Figure 4b). For either fresh electrodes or electrodes after 5 cycles, the SnO_2@C@TiO_2 shows the lowest impedance, implying that ultrathin C and TiO_2 coatings are conducive to charge transfer.

To further confirm the electrochemical kinetics, CV profiles are collected at various scan rates for the three SnO_2-based samples (Figure 4c and Figure S9). Increasing scan rate leads to more intense anodic peak and shift of the peak to higher potentials due to polarization. The capacitive contribution can be quantified by the following Equation 1:

$$i = av^b \quad (1)$$

where i and ν refer to the peak current and scan rate, a and b are adjustable values. The linear relationship between $\log i$ and $\log v$ can be used to determine the b-value. The b-value reflects the charge-storage mechanism, and the b-value of 0.5 and 1.0 indicates diffusion-limited and capacitive processes, respectively. The fitted b-values for SnO_2@C@TiO_2, SnO_2@C, and SnO_2 are 0.81, 0.81, and 0.63, respectively (Figure 4d). The above results signify that the Na storage process in SnO_2@C@TiO_2 and SnO_2@C is mainly capacitive controlled.[33,34]

Ex situ XRD is employed to study the structure evolution of SnO_2@C@TiO_2 (**Figure 5**). When discharged to 1.0 V, two peaks for SnO appear, while the peaks for SnO_2 become invisible (Equation 2). Upon deep discharging to 0.5 and 0.25 V, peaks for metallic Sn begin to appear, and the diffractions for SnO still exist (Equation 3). No diffractions for Na_2O can be observed, suggesting that the Na_2O may exist in its amorphous form.[35] At the end of discharge, the diffractions for SnO totally disappear, and the Sn signals weaken, indicating the complete conversion of SnO to Sn and its further alloying reaction with Na (Equation 4). Besides the peaks for Sn, another two peaks, which may be associated with Na_xSn, can also be discerned in the XRD pattern of the discharge products. Upon charging, the diffractions for SnO_2 re-emerge at 1.0 V. Upon further charging to 2.0 V, the XRD pattern recovers to its original state. According to the above discussion, the Na storage mechanism of SnO_2 can be described as follows:

$$SnO_2 + 2Na^+ + 2e^- \leftrightarrow SnO + Na_2O \quad (2)$$

$$SnO + 2Na^+ + 2e^- \leftrightarrow Sn + Na_2O \quad (3)$$

$$Sn + xNa^+ + xe^- \leftrightarrow Na_xSn \quad (4)$$

3. Conclusions

In summary, three-layer structured SnO_2@C@TiO_2 hollow spheres have been constructed. When employed in Na storage, the unique hollow structure not only provides short Na^+ diffusion paths, but also successfully prevents structural collapse caused by volume change. In addition, the introduction of carbon and the oxygen vacancies enhance the reaction kinetics. As a result, the SnO_2@C@TiO_2 hollow spheres demonstrate a capacity of ~ 381 mAh g^{-1} at 0.2 A g^{-1} with good durability. This structure design greatly improves the reversibility of SnO_2 in SIBs. This study offers an intriguing method to boost the Na storage performance of anode materials suffering from low conductivity and large volume variations.

4. Experimental Section

4.1.1. Synthesis of SnO_2 Hollow Spheres

The SnO_2 hollow spheres were fabricated by a hydrothermal method reported previously.[25]

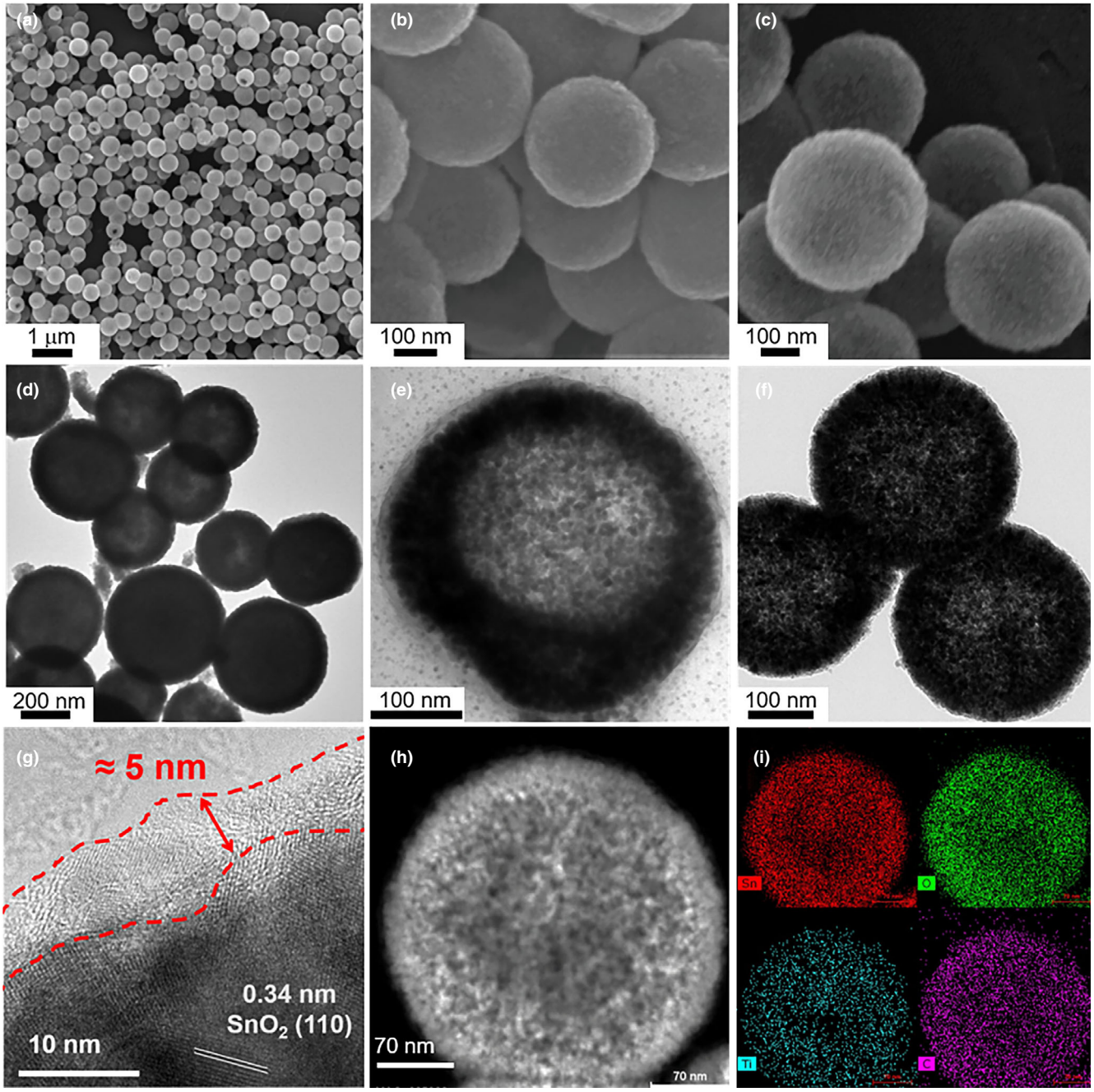

Figure 2. SEM images of a) SnO_2 , b) SnO_2@C , and c) SnO_2@C@TiO_2 ; TEM images of d) SnO_2 , e) SnO_2@C, and f) SnO_2@C@TiO_2; g) HRTEM image, h) STEM image, and i) the corresponding EDS mappings of SnO_2@C@TiO_2.

Synthesis of SnO_2@C Hollow Spheres

For carbon coating, 300 mg of as-prepared SnO_2 hollow spheres was dispersed in 120 mL Tris-buffer solution (10 mM). After that, 75 mg dopamine hydrochloride was added and kept stirring at 25 °C for 4 h. The obtained SnO_2@PDA hollow spheres were carbonized at 600 °C for 2 h in Ar to fabricate the SnO_2@C.

Synthesis of SnO_2@C@TiO_2 Hollow Spheres

To obtain SnO_2@C@TiO_2 hollow structures, 100 mg SnO_2@C was dispersed in 100 mL HCl (0.1 M), and then, 3 mL titanium(IV) bis(ammonium lactato)dihydroxide (Ti-BALDH, 50 wt% solution in water) was added. After stirring for 3 h, the resulting particles were then heated at 350 °C for 4 h in H_2 (5%)/Ar (95%). The

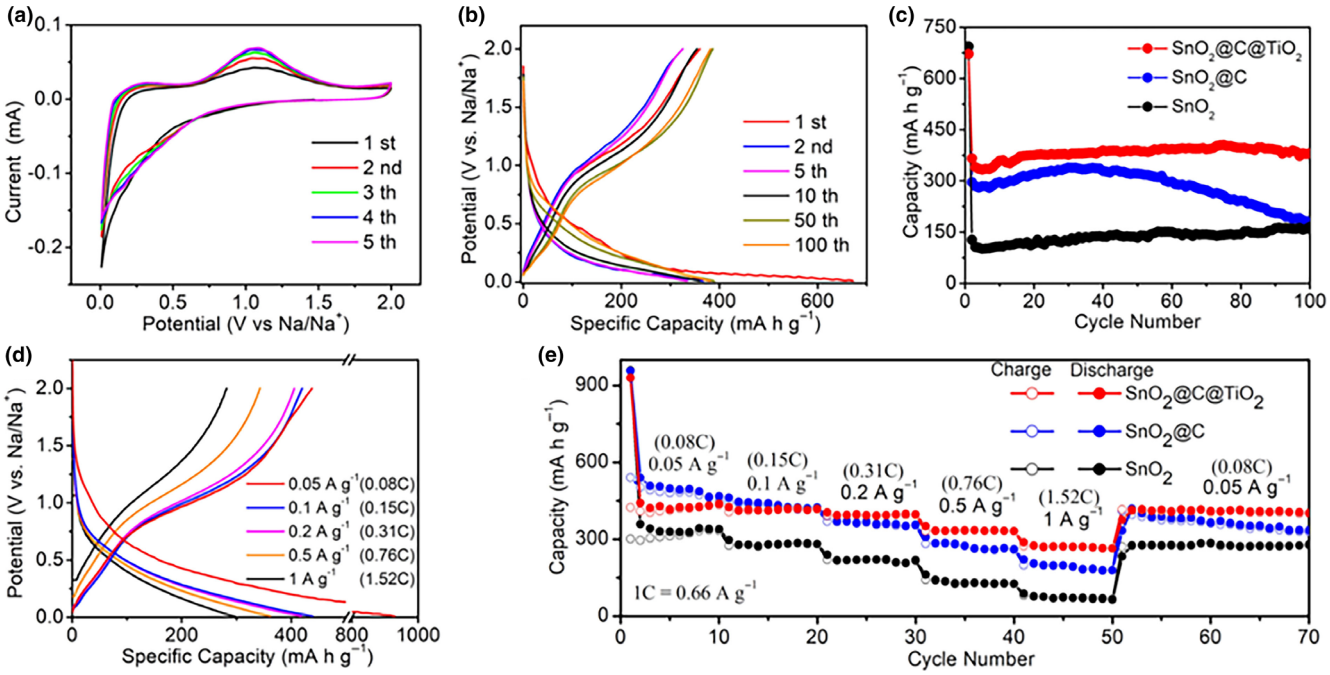

Figure 3. Electrochemical performances: a) CV curves of SnO_2@C@TiO_2 at 0.1 mV s^{-1}; b) GCD profiles of SnO_2@C@TiO_2 at 0.2 A g^{-1}; c) cycling performances of the three SnO_2-based samples at 0.2 A g^{-1}; d) GCD profiles of SnO_2@C@TiO_2 at different current densities and; e) rate performances of the three SnO_2-based samples.

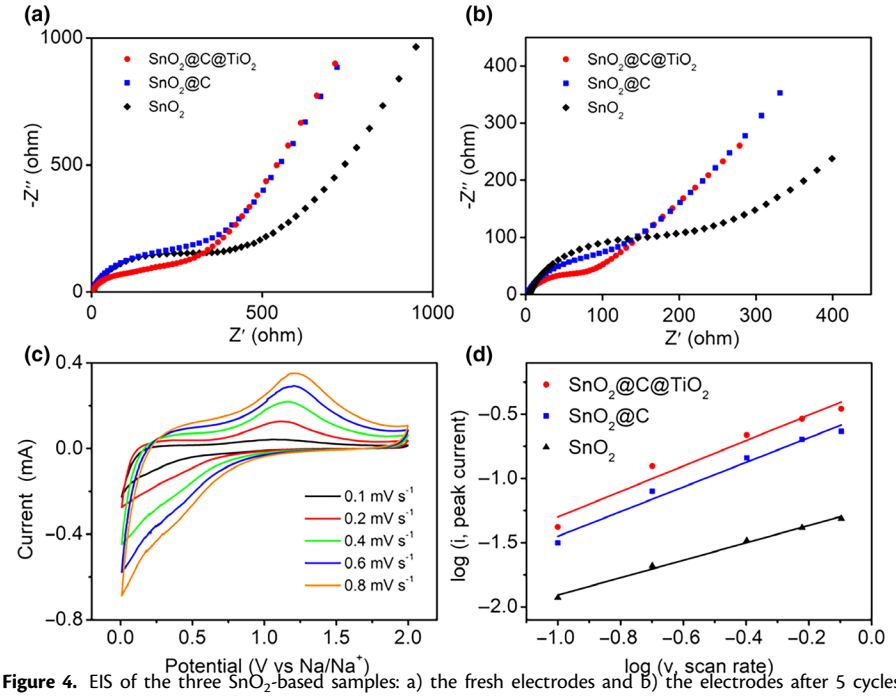

Figure 4. EIS of the three SnO_2-based samples: a) the fresh electrodes and b) the electrodes after 5 cycles at 2 V; c) CV profiles of SnO_2@C@TiO_2 in the potential range of 0.01–2.0 V at various scan rates; d) log(i) versus log(*v*) plots for the three SnO_2-based samples.

control sample, SnO_2@TiO_2, was prepared by the same synthesis recipe as SnO_2@C@TiO_2 without the introduction of dopamine hydrochloride.

Characterizations

XRD patterns were obtained by a D8 Discover X-ray diffractometer with Cu K_α X-ray source (λ = 1.5418 Å). SEM images were conducted using a JEOL JSM-7100F with an acceleration voltage of 20 kV. TEM, high-resolution TEM, and SAED patterns were conducted by using a Titan G2 microscope. TGA curves were carried out using a thermogravimetric analyzer. XPS spectra were obtained on a 2000 X-ray photoelectron spectrometer.

Electrochemical Measurement

The electrochemical measurements were evaluated in CR2016 type coin cells. The working electrode was composed of 70 wt.% active materials, 20 wt.% super P, and 10 wt.% carboxymethyl cellulose (CMC) binder. The slurry were coating on copper foil and dried, with a areal mass loading of ~ 1 mg cm^{-2}. Sodium metal foil was used as the counter electrode. The Whatman GF/A was used as separator. The electrolyte was 1 M $NaClO_4$ in propylene carbonate (PC) with 5% fluoroethylene carbonate (FEC). GCD measurements (0.01 – 2.0 V) were carried out with a LAND CT2001A multichannel battery testing system. CV and EIS were recorded on Auto laboratory electrochemical workstation.

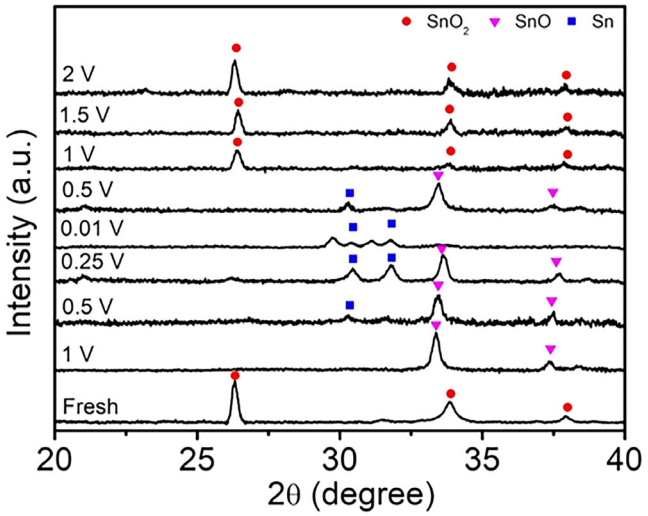

Figure 5. *Ex situ* XRD patterns of SnO_2@C@TiO_2 at 0.05 A g^{-1} between 0.01 and 2.0 V.

Acknowledgements

This work was financially supported by Shenzhen Fundamental Research Program (JCYJ20190809114409397).

Conflict of Interest

There are no conflicts of interest to declare.

Supporting Information

Supporting Information is available from the Wiley Online Library or from the author.

Keywords

hollow sphere, SnO_2, sodium-ion battery, protecting shell, structural integrity

Received: June 23, 2020
Revised: July 27, 2020
Published online: August 2, 2020

[1] J. Ding, H. Zhou, H. Zhang, T. Stephenson, Z. Li, D. Karpuzov, D. Mitlin, *Energy Environ. Sci.* **2017**, *10*, 153.
[2] J. Wu, Y. Cao, H. Zhao, J. Mao, Z. Guo, *Carbon Energy* **2019**, *1*, 57.
[3] Z. Yan, H. Jin, J. Guo, *Carbon Energy* **2019**, *1*, 246.
[4] T. Zhu, P. Hu, X. Wang, Z. Liu, W. Luo, K. A. Owusu, W. Cao, C. Shi, J. Li, L. Zhou, L. Mai, *Adv. Energy Mater.* **2019**, *9*, 1803436.
[5] T. Zhu, P. Hu, C. Cai, Z. Liu, G. Hu, Q. Kuang, L. Mai, L. Zhou, *Nano Energy* **2020**, *70*, 104548.
[6] J. Liang, J. Li, F. Zhang, X. Ding, J. Zapien, Y. Tang, *Batteries & Supercaps* **2019**, *2*, 440.
[7] S. Zhao, B. Qin, K. Chan, F. Li, *Batt. Supercaps* **2019**, *2*, 725.
[8] C. Cai, P. Hu, T. Zhu, C. Chen, G. Hu, Z. Liu, Y. Tian, Q. Chen, L. Zhou, L. Mai, *J. Phys. Energy* **2020**, *2*, 025003.
[9] S. Bublil, M. Fayena-Greenstein, M. Talyanker, N. Solomatin, M. N. Tsubery, T. Bendikov, T. R. Penki, J. Grinblat, I. B. Durán, I. Grinberg, Y. Ein-Eli, Y. Elias, P. Hartmann, D. Aurbach, *J. Mater. Chem. A* **2018**, *6*, 14816.
[10] T. Ma, X. Yu, H. Li, W. Zhang, X. Cheng, W. Zhu, X. Qiu, *Nano Lett.* **2017**, *17*, 3959.
[11] L. Shi, Y. Li, F. Zeng, S. Ran, C. Dong, S. Y. Leu, S. T. Boles, K. H. Lam, *Chem. Eng. J.* **2018**, *356*, 107.
[12] Y. Wang, C. Wang, Y. Wang, H. Liu, Z. Huang, *J. Mater. Chem. A* **2016**, *4*, 5428.
[13] M. Wang, X. Wang, Z. Yao, W. Tang, X. Xia, C. Gu, J. Tu, *ACS Appl. Mater. Inter.* **2019**, *11*, 24198.
[14] Y. Yan, Z. Pan, Y. Wang, Y. Ma, C. Li, Y. Lu, X. Wu, *Nanoscale* **2019**, *11*, 14616.
[15] H. Bian, X. Xiao, S. Zeng, M. F. Yuen, Z. Li, W. Kang, D. Yu, Z. Xu, J. Lu, Y. Li, *J. Mater. Chem. A* **2017**, *5*, 2243.
[16] Z. Li, J. Ding, H. Wang, K. Cui, T. Stephenson, D. Karpuzov, D. Mitlin, *Nano Energy* **2015**, *15*, 369.
[17] M. Y. Wang, X. L. Wang, Z. J. Yao, D. Xie, X. H. Xia, C. D. Gu, J. P. Tu, *J. Colloid Interf. Sci.* **2019**, *560*, 169.
[18] Q. Tian, Y. Chen, W. Zhang, Z. Sui, L. Yang, *J. Alloy. Compd.* **2019**, *820*, 153404.
[19] H. Zhang, X. Huang, O. Noonan, L. Zhou, C. Yu, *Adv. Funct. Mater.* **2017**, *27*, 1606023.
[20] Q. Wu, Q. Shao, Q. Li, Q. Duan, Y. Li, H. Wang, A. C. S. Appl, *Mater. Interfaces* **2018**, *10*, 15642.
[21] X. Lu, G. Wu, Q. Xiong, H. Qin, Z. Ji, H. Pan, *Electrochim. Acta* **2017**, *245*, 587.
[22] Z. Yi, Q. Han, P. Zan, Y. Cheng, L. Wang, *J. Mater. Chem. A* **2016**, *4*, 12850.
[23] Q. Tian, L. Li, J. Chen, L. Yang, S. Hirano, *J. Power Sources* **2018**, *376*, 1.
[24] G. J. Zhu, F. Z. Zhang, X. M. Li, W. Luo, L. Li, H. Zhang, L. J. Wang, Y. X. Wang, W. Jiang, H. K. Liu, S. X. Dou, J. P. Yang, *Angew. Chem. Int. Ed.* **2019**, *58*, 6669.
[25] X. Lou, Y. Wang, C. Yuan, J. Lee, L. Archer, *Adv. Mater.* **2006**, *18*, 2325.
[26] K. E. DeKrafft, C. Wang, W. Lin, *Adv. Mater.* **2014**, *2012*, 24.
[27] D. Ma, Y. Li, H. Mi, S. Luo, P. Zhang, Z. Lin, J. Li, H. Zhang, *Angew. Chem. Int. Ed.* **2018**, *57*, 8901.
[28] M. Shao, J. Liu, W. Ding, J. Wang, F. Dong, J. Zhang, *J. Mater. Chem. C* **2019**, *8*, 487.
[29] W. Tao, M. Wang, B. Zhu, W. Huo, R. Yang, H. Xiong, H. Tang, Z. Wei, Y. Wang, *Electrochim. Acta* **2020**, *334*, 135569.
[30] Y. Cheng, Q. Li, C. Wang, L. Sun, Z. Yi, L. Wang, *Small* **2017**, *13*, 1701993.
[31] J. Liu, L. Yu, C. Wu, Y. Wen, K. Yin, F. K. Chiang, R. Hu, J. Liu, L. Sun, L. Gu, J. Maier, Y. Yu, M. Zhu, *Nano Lett.* **2017**, *17*, 2034.
[32] C. Gao, Z. Jiang, P. Wang, L. R. Jensen, Y. Zhang, Y. Yue, *Nano Energy* **2020**, *74*, 104868.
[33] K. Liu, S. Tan, J. Moon, C. J. Jafta, C. Li, T. Kobayashi, H. Lyu, C. A. Bridges, S. Men, W. Guo, Y. Sun, J. Zhang, M. P. Paranthaman, X. Sun, S. Dai, *Adv. Energy Mater.* **2020**, *10*, 2000135.
[34] G. Liang, Y. Wang, Z. Huang, F. Mo, X. Li, Q. Yang, D. Wang, H. Li, S. Chen, C. Zhi, *Adv. Mater.* **2020**, *32*, 1907802.
[35] J. Patra, P. C. Rath, C. H. Yang, D. Saikia, H. Kao, J. Chang, *Nanoscale* **2017**, *9*, 8674.

